Politecnico di Torino

Politecnico di Torino

Master's Degree in Environmental and Land engineering

Climate Change

March 2026

Estimation of Design Rainfall under Climate Change Scenarios: A Case Study in Trieste

Supervisors:
Paola Mazzoglio
Pierluigi Claps

Candidate:
Petri Mattia

Abstract

The intensification of the hydrological cycle driven by anthropogenic warming represents a critical challenge for the resilience of civil infrastructure. Traditional hydraulic design, based on the assumption of climate stationarity, is increasingly proving to be inadequate to correctly represent the future frequency of extreme weather events. This thesis develops future Intensity-Duration-Frequency (IDF) curves for the RCP 4.5 and RCP 8.5 scenarios in Trieste, utilizing the VHR-PRO_IT Convection-Permitting Model (CPM) at a 2.2 km spatial resolution. Future IDF curves were derived based on the Gumbel distribution, averaging the results obtained with both Maximum Likelihood Estimation (MLE) and L-Moments. Results indicate a significant intensification of short-duration rainfall extremes: for a 10-year return period, rainfall intensity is projected to increase by approximately +60% (RCP 4.5) and +64% (RCP 8.5) compared to the historical baseline. In the case study considered in this work. The hydraulic analysis revealed that the existing network would fail in approximately 50% of pipe sections under these conditions. The proposed adaptation strategy, based on upgrading critical sections, proved effective in restoring hydraulic safety, requiring an additional investment of 20-21% compared to the baseline infrastructure cost. Finally, the study emphasizes the need to adopt multi-model ensemble approaches in future research to better quantify epistemic uncertainty.

Table of Contents

List of Figures

List of Tables

1. Introduction

The intensification of the global hydrological cycle represents one of the most critical and confident predictions of modern climate science in response to anthropogenic warming. As stated by the Intergovernmental Panel on Climate Change (IPCC), there is unequivocal evidence that human influence has warmed the globe, leading to widespread and rapid changes in the frequency and intensity of extreme weather events [1].

This phenomenon poses a significant challenge to the safety and resilience of hydraulic infrastructures, which have historically been designed under the assumption of a stationary climate. The physical driver of this intensification is primarily governed by the Clausius-Clapeyron (C-C) thermodynamic relationship in $Eq.(1)$ [2]:

$$\frac{de_s}{e_s} = \frac{L}{R_v \cdot T^2} dT \ , \qquad Eq.(1)$$

where e_s represents the saturation vapor pressure (describing the water-holding capacity of the atmosphere) as a function of temperature T. The other parameters involved in the equation are the latent heat of vaporization L and the specific gas constant for water vapor R_v.

By analysing this relationship, an increase in water-holding capacity of approximately 7% for every 1°C rise in temperature is observed. As the atmosphere warms, it can hold more moisture, which is then available to feed precipitating systems. While climate models predict a global mean precipitation increase of about 2-3 %/°C, the scaling of extreme rainfall is highly dependent on the event intensity and duration [3].

On a global average, this C-C scaling rate is consistent with satellite observations and reanalysis estimates [1], especially for daily precipitation. However, recent studies show that the C-C rate is often higher for short duration events (sub-daily extremes), sometimes reaching up to 14%/°C, due to dynamic feedbacks, like release in latent heat and intensified convective updrafts [4]. The sub-hourly extremes often exhibit the so-called “super C-C” scaling rate at lower temperatures (10-20 °C), but this rate tends to decrease at temperatures over 20°C [3].

As already mentioned, the design of civil infrastructures is strongly affected by climate change. Traditionally, the design of these infrastructures relies on Intensity-Duration-Frequency (IDF) curves, which are statistical tools derived from historical rainfall observations under the assumption of stationarity. This assumption states that statistical properties of precipitation, such as mean, variance and extremes, will remain constant in the future, mirroring those observed in the past. However, in a

warming climate, this assumption is no longer valid, making the historical data an insufficient predictor of future conditions [5].

To address this gap, there is the need to update IDF curves by incorporating climate change impacts. This transition requires moving from a purely statistical approach based on historical observations to a predictive approach that integrates outputs from Global and Regional Climate Models (GCMs and RCMs). Since deep convection typically occurs at a scale of a few kilometres, standard climate models with a horizontal resolution coarser than 10 km fail to resolve these processes explicitly and must rely on parametrization. To overcome this limitation, the use of high-resolution Convection-Permitting Models (CPMs), characterized by a resolution finer than 4 km, is becoming essential to accurately capture sub-daily convective extremes [4]. However, because CPMs are computationally expensive, they are typically applied only over limited regional domains. Furthermore, being relatively new tools, they can suffer from systematic errors, such as overestimating or underestimating peak rainfall intensities or dry periods in certain regions. For this reason, the application of bias correction techniques is a mandatory step before using CPM outputs for design purposes. By coupling these corrected climate projections with extreme value analysis, it's possible to derive future IDF curves suitable for the design of resilient hydrological infrastructure.

In response to these findings, national engineering guidelines are beginning to evolve to incorporate climate change considerations.

The methodologies currently employed to update IDF curves under climate change conditions can be broadly classified into four main categories [3]:

- **Simple Constant Percentage Increase**: this is the simplest and most widely adopted approach in current design standards. It involves applying a fixed scaling factor to the historical rainfall intensities. Well known examples of this approach include the United Kingdom and Belgium, where an increment of 20% and 30%, respectively, has been historically recommended for all rainfall extremes [3].
- **Adaptive Percentage Increase**: this method is an evolution of the simple constant percentage increase, and it involves the application of a variable safety factor depending on various parameters, such as temperature increase, time horizon and rainfall frequency. In Denmark, percentage increases of 20%, 30%, and 40% are considered for 2, 10- and 100 years as return periods [6]. This methodology has recently overcome previous guidelines based on the constant percentage increase in different countries. In fact, the UK adopted incremental rates depending on the time horizon (up to 10%, 20%, and 40% by 2040, 2070, and 2115, respectively).

- **Percentage Increases Based on the Clausius-Clapeyron Relationship**: in this method, a percentage increase based on the projected temperature increase is applied to rainfall intensities. The C-C rate R_{SC} is used in $Eq.(2)$ to correct the reference rainfall intensity I_{ref}, considering the temperature increase ΔT, obtaining the future rainfall intensity I_{fut}.

$$I_{fut} = I_{ref} \cdot \left(\frac{100 + R_{SC}}{100}\right)^{\Delta T} \quad , \qquad Eq.(2)$$

  The Canadian Standard Association recommends a value of 7%/°C for R_{SC}, but it's important to remark that a higher rate may be applied for short duration events, depending on the area of interest.

- **Future IDF Curves through Climate Models**: probably the most modern method, it involves the derivation of future Intensity-Duration-Frequency (IDF) curves, based on the rainfall extremes projected by climate models. Given this, future IDF curves are strongly related to the selected climate model, whose resolution can be too coarse to correctly represent reliable regional data.

However, a significant gap often remains between the advancing climate science and its practical application in design standards. While some jurisdictions have introduced simplified scaling factors to adjust design rainfall, these are frequently issued as advisory recommendations rather than mandatory requirements. Furthermore, even when applied, these static adjustments (fixed percentage increases) may fail to capture the complex intensification of sub-daily extremes [4].

From an economic and planning perspective, updating IDF curves to account for non-stationarity implies that future infrastructures will require larger initial investments to ensure adequate resilience. Nevertheless, recent literature emphasizes that these proactive adaptation strategies yield long-term economic benefits, as conceptually shown in Figure 1.

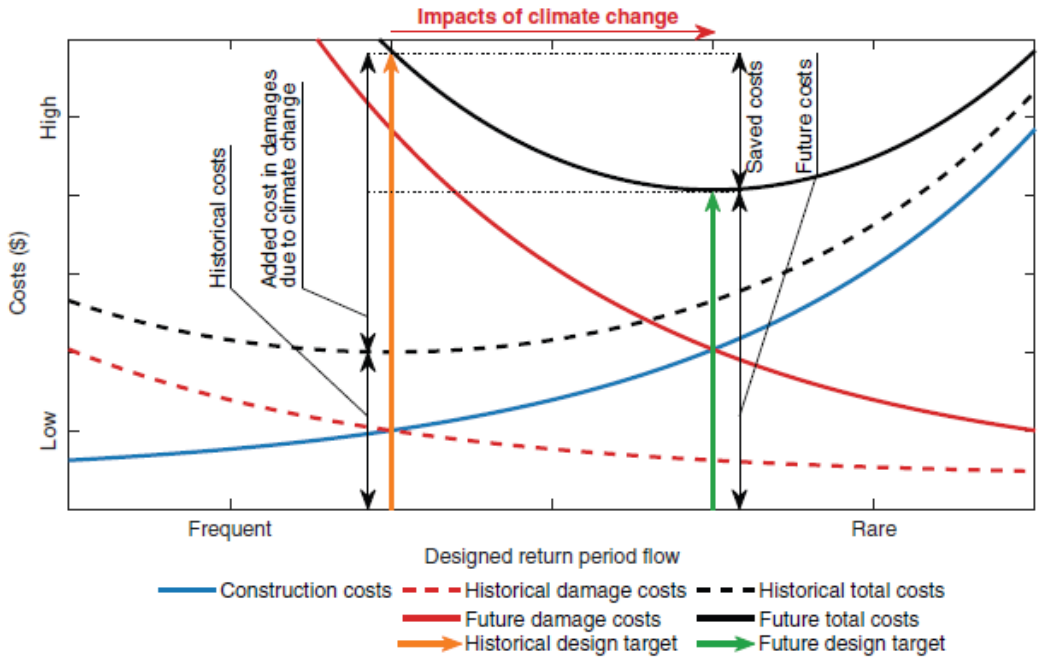

Figure 1: Conceptual representation of economic benefits associated with climate change adaptation [3].

While the initial construction costs are higher, the overall lifecycle cost is significantly reduced compared to a "do-nothing" scenario, where the economic impact of future flood damages and emergency repairs would far exceed the initial savings [3].

This work presents an application of a statistical methodology to derive future IDF curves under different climate scenarios. Through the case study of a drainage system, the analysis quantifies how the projected variations in rainfall intensity affect the hydraulic performance of the network and determines the consequent adaptation costs.

2. Methodology

This chapter outlines the theoretical and methodological framework adopted to analyse extreme precipitation events under both historical and future climate conditions. The approach combines statistical hydrology with climate modelling to derive robust design parameters.

2.1. Extreme Value Theory

Extreme Value Theory (EVT) provides the statistical framework for the analysis of rare hydrological events, enabling the modelling of the tails of probability distributions. Unlike traditional statistics that focus on the central tendency of data (averages), EVT specifically addresses the behaviour of extreme deviations [7].

2.1.1. Annual Maximum Series

EVT is typically applied to the maximum values of a timeseries, such as the annual precipitation maxima. The common way to get the Annual Maximum Series (AMS) is to apply the "block maxima" approach, which involves considering a block of one year and extract from it the maximum value. Same process is applied to different blocks and the AMS is obtained [8].

2.1.2. Probability distributions

A probability distribution describes the probability, for a particular value (e.g., rainfall depth) to occur in the sample space [9]. Given this, the next step is to fit a theoretical probability distribution to the data (AMS in this study). According to EVT, the distribution of AMS converges asymptotically to the Generalized Extreme Value (GEV) distribution. The Gumbel distribution, also used in this study, belongs to this family [8]. In addition to the EVT-based distributions, the Log-Normal distribution was included in the performance comparison. While the Log-Normal model is not derived from asymptotic extreme value theory, it is widely recognized in hydrological literature for its ability to represent precipitation data [10].

The probability distributions involved in this study are presented below:

1. **Generalized Extreme Value (GEV)** [11]: as previously mentioned, this is a flexible three-parameter distribution, which other distributions can be derived from. The Cumulative Distribution Function (CDF) of the variable z is defined as:

$$F(z) = exp\left\{-\left[1 + \xi\left(\frac{z-\mu}{\sigma}\right)\right]^{-\frac{1}{\xi}}\right\}, \qquad Eq.(3)$$

where:

- μ: location parameter, describing the centre of the distribution.
- σ: scale parameter (σ >0), describing the width or dispersion of a distribution.
- ξ: shape parameter governing the tail behaviour of the distribution.

2. **Gumbel distribution**: it corresponds to a limit case of the GEV in which the shape parameter approaches zero (ξ=0). Its CDF is represented in $Eq.(4)$, where it can be noted that it requires the fitting of only 2 parameters.

$$F(z) = exp\left\{-exp\left[-\left(\frac{z-\mu}{\sigma}\right)\right]\right\} \qquad Eq.(4)$$

Gumbel distribution is often more robust than the GEV when the sample size is small, reducing the uncertainty in quantile estimation [12].

3. **Log-Normal** [10]: this distribution assumes that the natural logarithm of the variable z follows a normal distribution. Unlike the previous cases, the Log-Normal CDF is not expressed in a simple algebraic form, therefore the Probability Density Function (PDF) of z is reported in $Eq.(5)$ [13], which is simply the derivate of the CDF. For this reason, the CDF can be obtained by integrating the PDF, usually via numerical methods.

$$f(z) = \frac{1}{z \cdot \sqrt{\sigma_y^2 2\pi}} exp\left[-\frac{\left(ln\,(z) - \mu_y\right)^2}{2\sigma_y^2}\right], \qquad Eq.(5)$$

where:

- μ_y: mean of the logarithm of the data, it determines the scale parameter
- σ_y: standard deviation of the logarithm of the data (shape parameter)

2.1.3. Parameters Estimation

Once the probability distribution models (GEV, Gumbel, and Log-Normal) were defined, the next step involved is estimating their parameters based on the AMS. Two different approaches will be employed in this work:

1. **Maximum Likelihood Estimation (MLE):** this method is widely used in hydrological frequency analysis [14], which seeks to find the set of parameters that maximizes the log-likelihood function $l(\theta)$, defined as:

$$l(\theta) = ln\big(L(\theta)\big) = \sum_{i=1}^{m} ln\big(f(z_i;\theta)\big), \qquad Eq.(6)$$

where:

- L is the likelihood function;
- m is sample size of AMS;
- θ is the set of parameters to be estimated.

The set of parameters for which $l(\theta)$ is maximized is then used in the probability distribution function.

2. **Method of L-Moments**: studies revealed that this alternative method provides reliable results in modelling extreme values [15]. This approach is grounded in the theory of Probability-Weighted Moments (PWM), which characterize a probability distribution through the moments of its order statistics. To estimate these moments from a finite sample of size m, unbiased estimators b_r are computed from the ordered sample $z_1 \leq z_2 \ldots \leq z_m$, given by [16]:

$$b_r = \frac{1}{m} \cdot \sum_{i=1}^{m} \frac{(i-1)(i-2)\ldots(i-r)}{(m-1)(m-2)\ldots(m-r)} \cdot z_i \qquad Eq.(7)$$

These estimators are linear combinations of the order statistics and are known to be robust to outliers and unbiased.

Up to three L-moments will be employed for the involved probability distributions which are here expressed:

$$L_1 = b_0, \qquad Eq.(8)$$

$$L_2 = 2b_1 - b_0, \qquad Eq.(9)$$

$$L_3 = 6b_2 - 6b_1 + b_0, \qquad Eq.(10)$$

Consecutively, location μ, scale σ and shape ξ can be obtained thanks to the following equations for the three different probability distributions:

- GEV:

$$c = \frac{2}{3 + L_3/L_2} - \frac{log2}{log3}, \qquad Eq.(11)$$

$$\xi = 7.8590 \cdot c + 2.9554 \cdot c^2, \qquad Eq.(12)$$

$$\sigma = \frac{L_2 \xi}{\Gamma(1+\xi)(1-2^{-\xi})}, \qquad Eq.(13)$$

$$\mu = b_0 + \sigma \cdot \frac{\Gamma(1+\xi)-1}{\xi}, \qquad Eq.(14)$$

where c is just an intermediate variable and Γ is the gamma function.

- Gumbel ($\xi \to 0$):

$$\sigma = \frac{L_2}{ln2}, \qquad Eq.(15)$$

$$\mu = L_1 - 0.5772 \cdot \sigma, \qquad Eq.(16)$$

- Log-Normal [17]:

$$\sigma = \sqrt{2} \cdot erf^{-1}\left(\frac{L_2}{L_1}\right), \qquad Eq.(17)$$

$$\mu = ln(L_1) - \frac{\sigma^2}{2}, \qquad Eq.(18)$$

Where the error function erf is defined as:

$$erf(x) = \frac{2}{\sqrt{\pi}} \cdot \int_0^x e^{-t^2} dt \ , \qquad Eq.(19)$$

The comparison between these estimation techniques allows to balance statistical efficiency with robustness, ensuring that the selected parameters for the IDF curves are physically consistent with the observed hydrological extremes

2.1.4. Distribution Selection Criteria

Once the parameters have been selected for each of the probability distribution function, there's the need to quantitatively understand which of these models can go on with the precipitation analysis. Two different selection criteria have been found in the literature and are here presented [18]:

- **Akaike Information Criterion (AIC):** is based on the principle of maximum entropy and it's calculated for each operational model j using the equation:

$$AIC_j = -2\, ln\left(L_j(\theta)\right) + 2n, \qquad Eq.(20)$$

where *n* is the number of estimated parameters.

The criterion is a trade-off between the goodness-of-fit, represented by the first term, while the second term ($2n$) acts as a penalty for increasing model complexity (i.e., adding parameters). The model with the minimum AIC value is selected as the best one.

- **Anderson-Darling Test Statistic:** another method is employed in order to verify if results from AIC are consistent. The standard Anderson Darling test statistic Δ_{AD} is defined as:

$$\Delta_{AD} = -m - \frac{1}{m}\sum_{i=1}^{m}\left[(2i-1)\,ln\big(F(z_i)\big) + (2m+1-2i)\,ln\big(1-F(z_i)\big)\right], \qquad Eq.(21)$$

where m is the sample size of data (arranged in ascending order) and i is the position index of the data. Also for this case, the lower the Δ_{AD} is, the better the model fits the data.

The Anderson Darling statistic value identify only the goodness-of-fit of the evaluated model, without considering the different numbers of parameters involved, which, on the contrary, penalizes the AIC. An evolution of the proposed criterion exists, which includes the number of parameters (the ADC proposed by [18]), but in this work, a criterion based on the trade-off between goodness-of-fit and model complexity (AIC), and a criterion based only on the goodness-of-fit (Standard AD) will be used.

2.2. Return Period

The primary objective of frequency analysis is to estimate the precipitation magnitude, known as return level h_p associated with a specific return period T. The return period is defined as the average time interval between events of a certain magnitude, a concept not only applicable to precipitation, but also to floods and other extreme events [19]. Mathematically, h_p is obtained by inverting the cumulative distribution function $F(h)$ of the selected probability model (e.g., GEV or Gumbel) [20]. Graphically, this relationship is illustrated in Figure 2 which displays the CDF curve: the y axis represents the non-exceedance probability p, while the x-axis corresponds to the precipitation depth h (in mm). Once p is defined, the corresponding rainfall depth h_p is obtained through the inverse CDF.

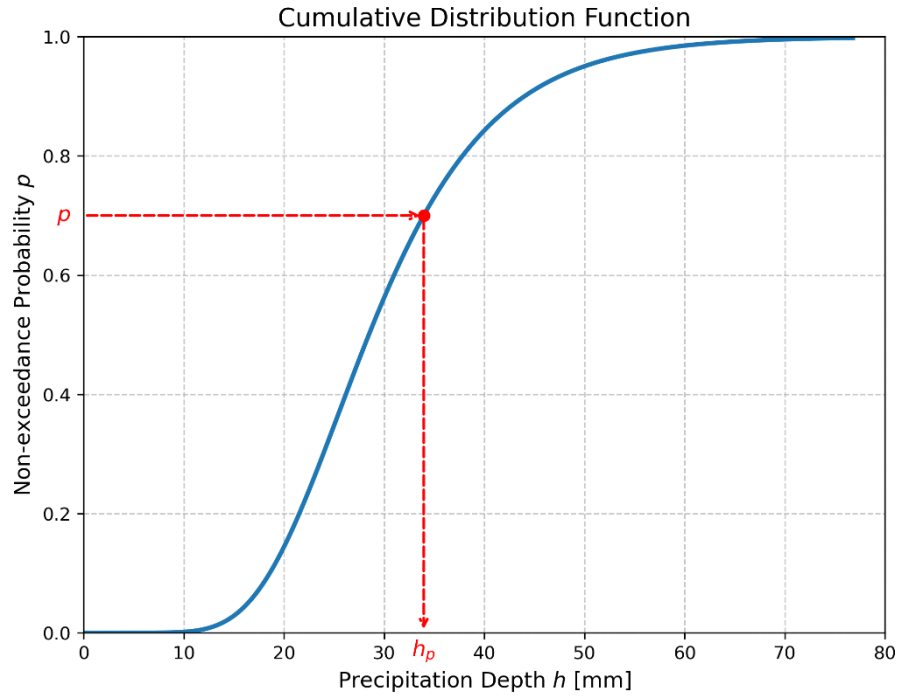

Figure 2: Cumulative Distribution Function (CDF) of Gumbel distribution correlating the selected non-exceedance probability to the precipitation depth.

The relationship between the return period T and the exceedance probability $(1-p)$ is given by:

$$T = \frac{1}{1-p} = \frac{1}{1-F(h_p)} \qquad Eq.(22)$$

The traditional definition of return period relies on the assumption of stationarity, implying that the statistical properties of extreme events remain constant over time. However, in the context of a warming climate, this assumption is increasingly challenged. The intensification of extreme rainfall is well documented and projected to continue, leading to non-stationarity. Projections from Global Climate Models (GCMs) indicate that events historically considered rare will become much more frequent. Specifically, on a global average, a rainfall intensity currently associated with a 20-year return period is projected to correspond to a 6-year return period in the future. This implies that infrastructure designed under historical stationary assumptions may face a risk of failure significantly higher than anticipated [3].

2.3. Intensity-Duration-Frequency (IDF) Curves

Intensity-Duration-Frequency (IDF) curves are a common tool used to design hydraulic engineering infrastructures. As the name says, they represent the intensity of precipitation (typically mm/h) against different event duration (from minutes to days), for different return periods (years) [3]. In

most cases, it is sufficient to cover durations from 5 min to 24 hours, and return periods from 2 to 200 years, in order to satisfy the needs of most engineering applications.

To construct these curves, the frequency analysis procedure described in the previous sections is repeated for multiple rainfall aggregation durations. Specifically, the Annual Maximum Series (AMS) is extracted for each duration of interest, and the selected probability distribution is fitted to each dataset to estimate the corresponding return levels (precipitation depth h). Once the precipitation depths are estimated, they are converted into rainfall intensities i as,

$$i = \frac{h}{d}, \qquad Eq.(23)$$

where d is the duration.

To obtain a continuous representation across all durations, an analytical function is fitted to the calculated discrete points in the intensity-duration plot. A widely used mathematical formulation is the simple power-law relation [21], expressed as,

$$i(d,T) = a \cdot d^{n-1}, \qquad Eq.(24)$$

where a and n are site-specific parameters, which depend on T.

2.4. Climate Models

Climate models are computational tools for understanding the Earth's climate system and, mostly important, predicting its future evolution. These tools serve to simulate the complex interactions between the components of the climate system, meaning atmosphere, hydrosphere, lithosphere, cryosphere, and biosphere, allowing scientists to study past, present, and future climate scenarios, assess the impact of anthropogenic activities on climate.

They are based on many balance equations that describe the physical principles governing the climate system. Just to mention some of them, there are equations of conservation of mass, momentum (Navier-Stokes equation) and energy, together with thermodynamic processes.

The Earth is divided into grid cells, and equations are solved numerically for each cell, which interacts with the surrounding ones.

2.4.1. General Circulation and Regional Climate Models

General Circulation Models (GCMs) are the primary tools for simulating the response of the global climate system. They simulate the physical processes on a global scale, with a coarse spatial

resolution (100-200 km), not permitting to catch small-scale meteorological phenomena, relevant to hydrology.

To bridge this scale gap, Regional Climate Models (RCMs) provide high-resolution simulations over limited geographical areas, delivering essential climate details for local impact studies. Through a process known as dynamical downscaling, RCMs use the GCM output as lateral boundary conditions to simulate the climate over a limited domain at a higher resolution (typically 12–50 km, such as in the EURO-CORDEX initiative).

While some interaction processes are straightforward to calculate by knowing the models state variables, others may require parameterisations. Parameterisation is a statistical relationship between the mean state variables of that specific grid cell and the forcing result from the unresolved physical processes [22]. Parameterisation is necessary for two main reasons:

- Resolution limit: many physical processes happen at a size smaller than the grid box, like cloud formation and convection, making the model grid too coarse to catch and solve explicitly these small processes.
- Computational power: parameterisation accounts for a large part of the computational power. However, without it, it would be required a massive amount of power to explicitly solve the small-scale phenomenon.

Despite RCMs resolution is improved compared to GCMs, they still rely on parameterization schemes to approximate deep convection, ie. thunderstorms, which may lead to underestimation of sub-daily rainfall extremes.

2.4.1. Convection Permitting Models

Recent advances in computing power have enabled the development of Convection-Permitting Regional Climate Models (CP-RCMs), which operate at kilometre-scale resolutions (<4 km). Unlike standard RCMs, these models explicitly resolve deep convection processes without relying on parameterization schemes, making them particularly valuable for precipitation analysis due to their high temporal resolution (hourly data) [3].

Specifically, this project utilizes the VHR-PRO_IT (Very High Resolution PROjections for ITaly) dataset [23]. This dataset was obtained by dynamically downscaling the regional climate model COSMO-CLM to a spatial resolution of 2.2 km over the Italian domain. This high resolution allows for a more accurate simulation of land-atmosphere feedbacks and the detection of surface heterogeneities, which are critical for capturing local meteorological phenomena [23]. It contains data

for an historical period 1989-2005, and two greenhouse gas concentration pathways (RCP 4.5 and RCP 8.5) for the future period 2006-2050.

It is important to note that the VHR-PRO_IT dataset is obtained from a single simulation, so it doesn't allow to evaluate the climate internal variability. It should be necessary an ensemble of CPMs over Italy, making it more intended for research purposes than decision-making or engineering activities. In any case, authors of VHR-PRO_IT dataset strongly recommend to apply bias correction techniques in order to remove systematic biases.

2.5. Bias Correction

Despite the sophisticated representation of the climate system, data output from climate models is affected by systematic errors, commonly referred to as biases. Models can simulate precipitation that occurs too often (the so-called "drizzle effect" in which light rainy days are overestimated and total amount of extreme events are underestimated [24]), while simultaneously underestimating the intensity of rainfall extremes. These inaccuracies are caused by limited spatial resolution, simplified thermodynamic processes, parameterisation, and the usage of uncorrected outputs can lead to unrealistic results [25].

Different bias correction techniques, and their variations, are present in literature and here are presented 4 established methods that have been tested and compared in [26]:

- Linear: this basic method involves the usage of a scaling factor a applied to the model output precipitation data P.

$$P^* = aP \qquad Eq.(25)$$

  where P^* is the corrected rainfall data.

  This method is also known in literature as "delta change" method.

- Non-linear: this technique is very similar to the linear one, but it adds a power law correction with the exponent b so that

$$P^* = aP^b \qquad Eq.(26)$$

- Distribution-based quantile mapping: it's a member of the Quantile Mapping (QM) family and is based on the comparison between the statistical distribution of the modelled and observed data. In mathematical terms, QM consists in firstly evaluating the quantile q associated with a simulated data using the Cumulative Distribution Function (CDF) of the modelled data (F_{mod}), as expressed in $Eq.(27)$. Then, the bias-corrected precipitation

value is obtained by computing the inverse CDF of the observed data (F_{obs}^{-1}) and apply it to the quantile previously obtained, as shown in $Eq.(28)$ [27] and schematically illustrated in Figure 3.

$$q = F_{mod}(P) \qquad Eq.(27)$$

$$P^* = F_{obs}^{-1}(q) \qquad Eq.(28)$$

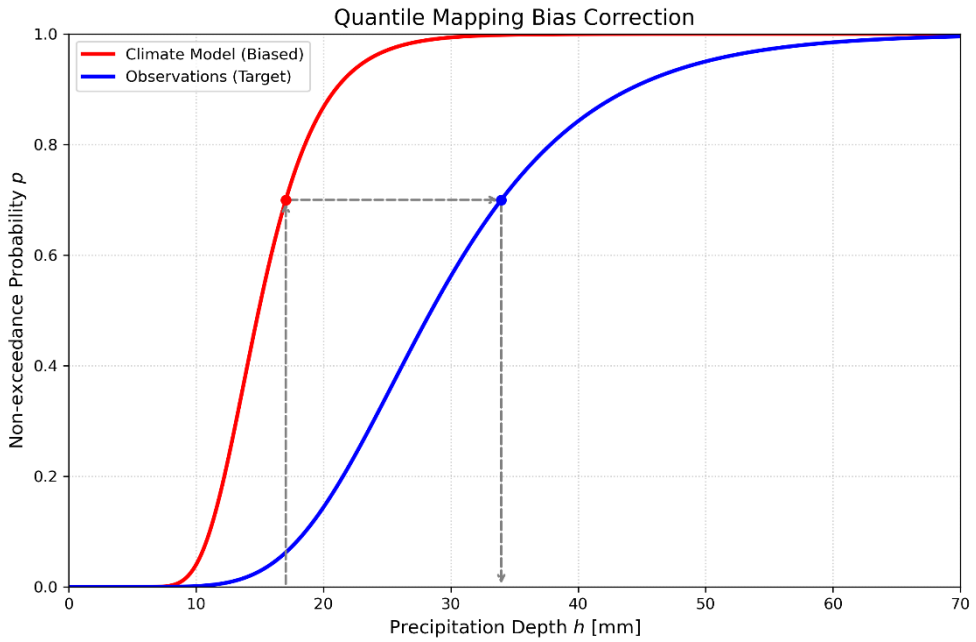

Figure 3: Schematic representation of the Distribution-based Quantile Mapping method.

From this general description, the distribution QM assumes that modelled and observed data follow a theoretical distribution selected a priori by the user. The same distribution family is generally adopted for both datasets, while the distribution parameters are estimated independently for the modelled and observed data.

- Empirical quantile mapping: it follows the same approach of the distribution Q, but, in contrast to it, it doesn't make any a priori assumption regarding the theoretical shape of the distribution. In this case, observed data is divided into specific discrete quantiles and, for each division, a linear correction factor is calculated as in $Eq.(25)$.

Among these methods employed in the comparison study [26], the author stated that the distribution QM (in his study he used Gamma-based QM) is identified as the best combination of accuracy and robustness. For this reason, in the further case study this bias correction method will be employed.

3. Case study

3.1. Site Location: Trieste

The area under investigation is located in Trieste (North-Eastern Italy), specifically within the industrial district of Servola. The site, historically occupied by a steelwork, is currently undergoing a significant redevelopment process (MISP project) involving a long-term containment of polluted groundwater using physical barriers and is preparatory to the construction of a new port infrastructure [28].

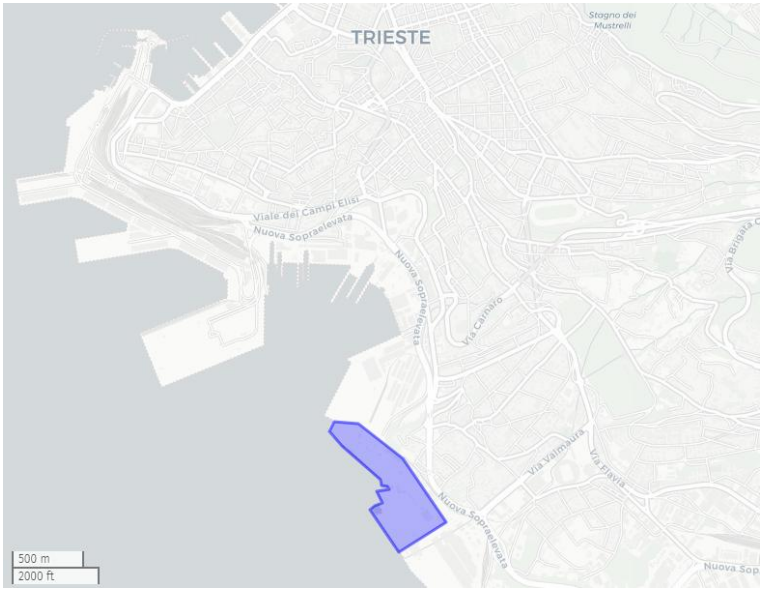

Figure 4: Area interested by MISP project.

Figure 4 shows the area of interest for the MISP project and for this work. Map was created using the online tool “uMap” [29].

From a geological perspective, the area is characterized by anthropogenic fill layers resulting from over a century of industrial activity. Consequently, concrete paving is necessary for environmental sealing purposes. As the resulting surface is considered entirely impermeable, a dedicated drainage system has been designed to manage surface runoff.

Regarding climatological characterization, the mean annual precipitation in Trieste is approximately 1000 mm. The precipitation regime exhibits a peak during the autumn months: the wettest period occurs from September to November, with monthly means between 110 and 130 mm [30]. In opposite, the driest month is March, with an average rainfall of approximately 55 mm.

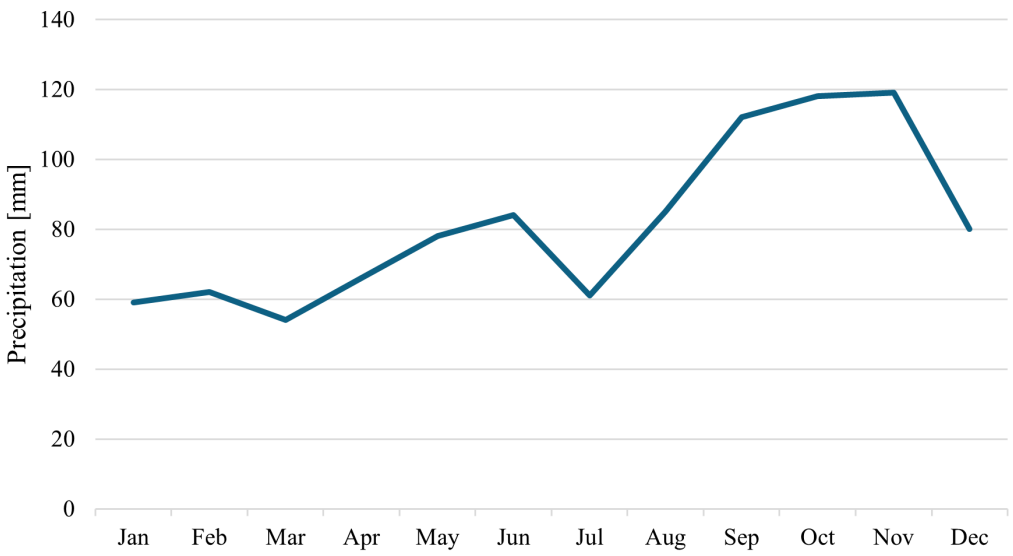

Figure 5: Average monthly precipitation in Trieste.

3.2. Rainfall data retrieval

3.2.1. Historical

The observational dataset used for the hydrological analysis was retrieved from the official archive of the *Friuli Venezia Giulia Region - Hydraulic and Mareographic Service*. The data repository is accessible via the regional online portal, allowing the selection of different measured data which, for this study, the maximum annual rainfall was selected [31].

The reference rain gauge for the study area was identified based on the executive hydraulic design report of the MISP project, and corresponds to the pluviometric station called “Trieste - Istituto Nautico" (station ID: S002), located in the city centre, but considered the most representative monitoring point due to its proximity to the site and length of recording history.

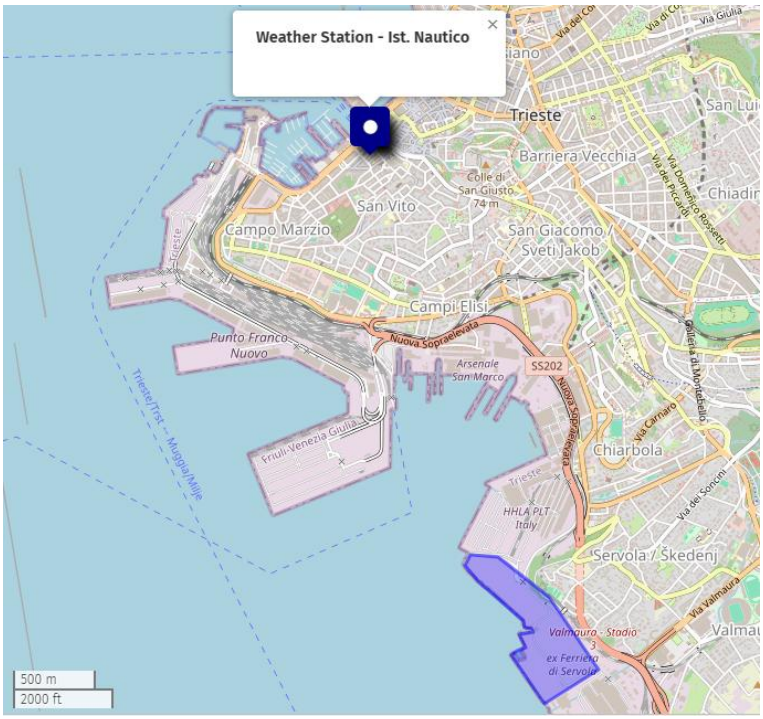

Figure 6: "Istituto Nautico" weather station location.

Due to unavailability of rainfall timeseries, the most adequate data format was in terms of Annual Maximum Series (AMS), already processed and available for direct download. The dataset covers a significant historical period spanning from 1919 to 2011, for durations ranging from 15 min to 120 hours. Figure 7 provides a visual overview of data availability across the investigated timeframe for three different durations.

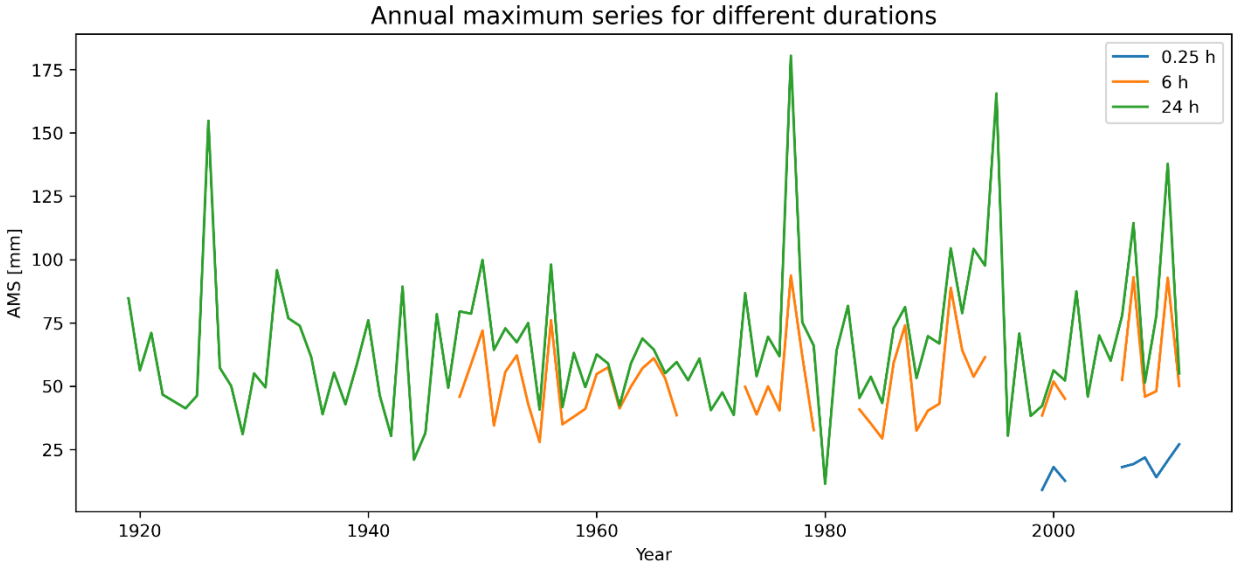

Figure 7: AMS for different durations of observed historical data.

As can be noted, the temporal coverage is not perfectly continuous; in fact, the timeseries exhibits occasional gaps and discontinuities, which may be attributable to temporary sensor failures or

maintenance periods. As reported in Table 1, sub-daily durations (1, 3, 6 and 12 h) share a nearly identical sample size, approximately 51 years. Similarly, for daily duration and above, the data availability is higher, equal to 92 years. Conversely, sub-hourly data is much less available.
Despite these interruptions, the remaining sample size will be used in the application of EVT.

Table 1: Data availability of observed historical AMS for different durations

Duration [h]	0.25	0.5	0.75	1	3	6	12	24	48	72	96	120
Years	10	14	24	51	51	51	53	92	92	92	92	92

The variability in data availability is also linked to the evolution of the monitoring technology. Historically, the observation network relied on traditional mechanical pluviographs, which required manual data extraction and often provided daily totals based on fixed observation intervals (from 9:00 AM to 9:00 AM) [32]. Conversely, the latter part of the record reflects the modernization of the monitoring system with the installation of electronic pluviographs. These electronic sensors allow for continuous high-frequency data logging, in this case 15 min time steps, allowing the calculation of a rolling window to identify the real AMS.
Regarding the 24-hour duration, the dataset most of the time provided dual records for the same year (likely corresponding to the fixed 9:00 AM –9:00 AM observation and the reconstructed sliding maximum). For this reason, the highest precipitation depth was selected, assuming it corresponds to the real 24-hour maximum.
In literature a way to correct the fixed time interval maxima is present, which involves the application of the Hershfield factor [33]. This factor is just a multiplier, typically equal to 1.13 for a 24-hour duration, aiming to compensate for the systematic underestimation caused by the discretization of continuous rainfall into fixed time intervals. While literature suggests this corrective factor, the official AMS dataset provided by the Regional Hydrographic Office was used for consistency throughout the entire observation period.

3.2.2. Climate model (VHR-PRO_IT)

Precipitation data from the VHR-PRO_IT CPM can be found online for a historical period from 1981 to 2005, and for a future period from 2006 to 2070 for both RCP 4.5 and RCP 8.5 climate projections [23]. The location of interest was selected (Lat=45.623°, Lon=13.777°, WGS 84 coordinate reference system) and the data was downloaded. In this case, the temporal resolution is hourly, so the AMS can be evaluated only for durations >1h. To be more precise, a rolling windows was used for hydrological durations of 1, 3, 6, 12, 24, 48, 72, 96 and 120 hours, as provided for the historical data from rain gauges.

It's important to remind that the extracted AMS is not directly used for the design, but it serves as the input for the bias correction, as explained in Section 2.5.

3.3. Statistical Analysis

3.3.1. Probability distribution selection

To determine the most suitable probability distribution model for representing the extreme rainfall in Trieste, a comparative analysis was performed on the AMS. Three families of probability distributions tested, i.e. GEV (3 parameters), Gumbel (2 parameters) and Log-Normal (2 parameters), and, for each, parameters were estimated using two different techniques, meaning Maximum Likelihood Estimation (MLE) and L-Moments.

The selection criteria were based on the values of AIC and AD, as discussed in Section 2.1.4, for each examined duration. Given the multi-duration nature of the dataset, a global ranking system was implemented. For each model, two aggregate scores were calculated:

- **Total AIC**: sum of AIC scores across all durations. A mean was not meaningful since AIC increases with duration.
- **Mean AD**: average Anderson-Darling statistic across all durations. In this case values were independent of durations.

The results were ranked in descending order (lower values of AIC and AD, better the model), so it was possible to determine the best probability distribution model among the others.

Same methodology was applied to the climate model historical data in order to understand if the best probability distribution model for one dataset was adequate also for the other one. If different distributions were used (e.g., GEV for observed and Gumbel for the model), the bias correction could introduce artifacts, especially when extrapolating to future scenarios.

Table 2 reports the results for the observed dataset and the historical model.

Table 2: Comparison of Akaike Information Criteria (AIC) and Anderson-Darling (AD) results by distribution

Historical observed				**Historical climate model**			
Model	AIC	**Model**	AD	**Model**	AIC	**Model**	AD
GUM_MLE	6415	**GEV_MLE**	0.499	**GUM_MLE**	1708	**GUM_LM**	0.418
GUM_LM	6418	**GUM_LM**	0.530	**LN_MLE**	1709	**LN_MLE**	0.420
GEV_MLE	6430	**GUM_MLE**	0.532	**GUM_LM**	1713	**GUM_MLE**	0.425
LN_MLE	6434	**LN_MLE**	0.631	**GEV_MLE**	1748	**GEV_LM**	0.820
LN_LM	6686	**GEV_LM**	1.026	**LN_LM**	1765	**LN_LM**	1.733
GEV_LM	inf	**LN_LM**	2.470	**GEV_LM**	inf	**GEV_MLE**	2.917

Given that the statistical ranking is not entirely consistent between the observed data and the historical climate model outputs, additional considerations were necessary to select a unified probability distribution.

Firstly, the GEV distribution fitted with L-Moments was excluded due to numerical inconsistencies. The resulting AIC was infinite, a condition that occurs when the fitted parameters imply an upper limit that is lower than the maximum observed precipitation, causing the likelihood function to diverge (logarithm of zero). Furthermore, AD was approximately 1.0, indicating a sub-optimal fit compared to other candidates.

Similarly, the Log-Normal distribution estimated via L-Moments was discarded due to consistently high AD values across both datasets.

Particular case is for GEV distribution using MLE method. While it provides a good fit for the observed dataset, it fails to accurately represent the historical climate model data, yielding excessively high AD scores. Specifically, for the 3-hour duration, the parameter estimation algorithm failed to converge to a physically realistic solution. As illustrated in Figure 8, while the GEV with L-Moments maintains stable parameters (left panel), the GEV with MLE (centre panel) yields an anomalous shape parameter of $\xi \approx 2.76$. This value is physically inconsistent with precipitation processes, for which values typically range between 0 and 0.23 [34].

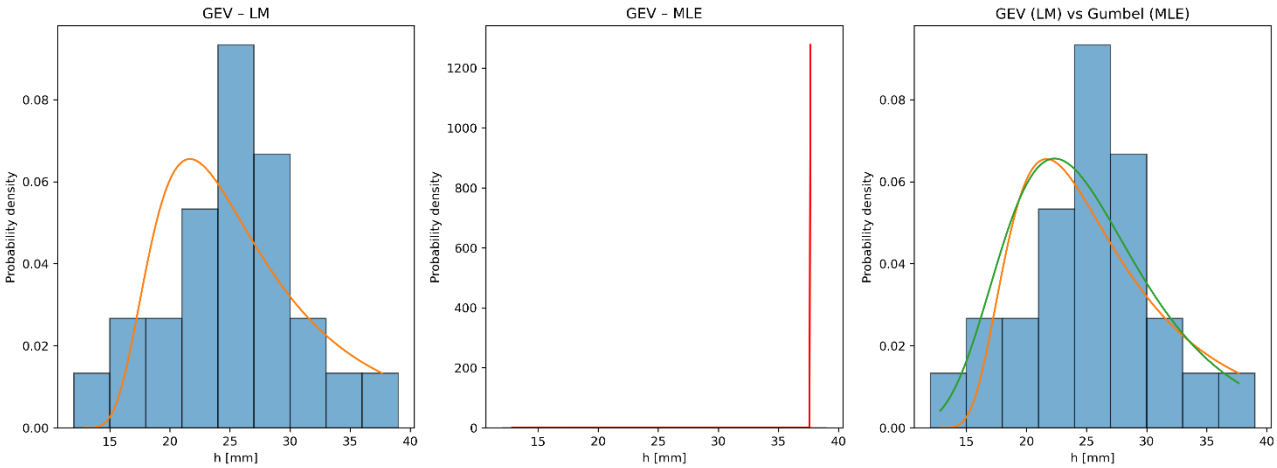

Figure 8: Probability distribution quality on CPM historical data: GEV with L-Moments (left), GEV with MLE (centre) and comparison of GEV with L-Moments and Gumbel with MLE.

Consequently, the Gumbel distribution was identified as the most robust and consistent model for the study. Since the results for AIC and AD obtained via MLE and L-Moments are nearly equivalent for this distribution, both methods were initially considered to assess the sensitivity of the projections to the statistical modelling choice. However, for the operational phase of the study, it was decided to have a single rainfall input. To avoid biasing the design toward one specific estimator, an ensemble approach was adopted. The final design IDF curves were derived by calculating the arithmetic mean (coincident with the median typically used in an ensemble of results [35]) of the rainfall intensities obtained from the MLE and L-Moments methods for each duration.

3.3.2. Bias correction of future data

As explained in Section 2.5, it's necessary to bias correct the climate model AMS for both future climate scenarios RCP 4.5 and RCP 8.5 in order to elaborate future IDF curves.

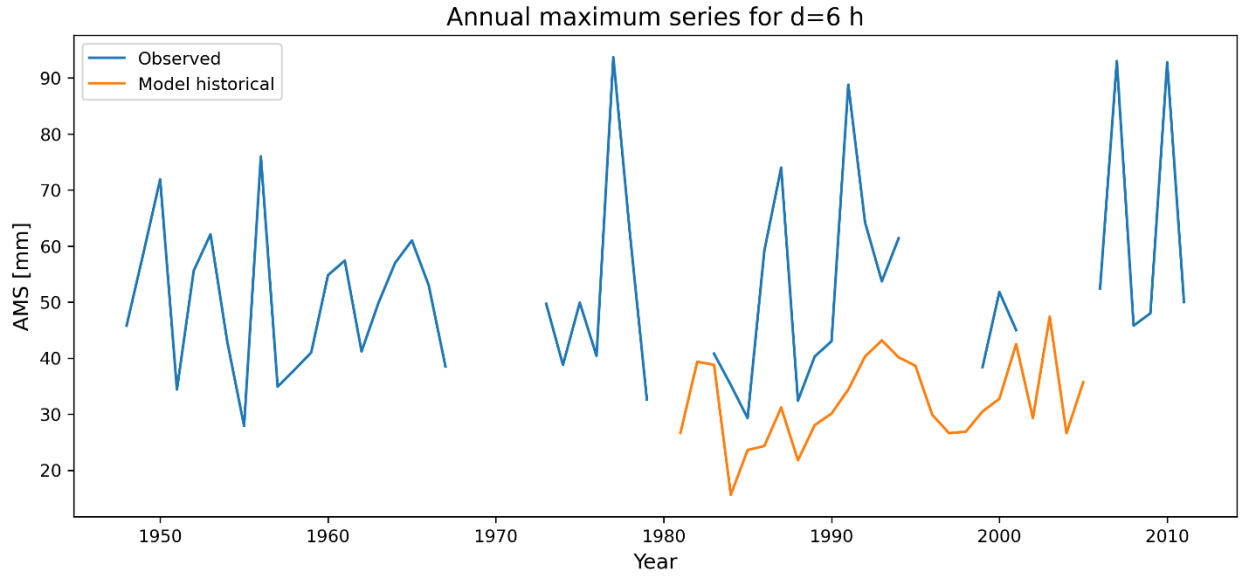

Figure 9: Annual maximum series for 6-hour duration from both observed and CPM historical dataset.

As an example, Figure 9 shows the AMS obtained from the observed dataset and the climate model historical one. It is evident that a bias is present, confirming the need of bias correction.

Regarding the temporal mismatch between the climate model simulation (1981–2005) and the observed series (1919–2011), the entire observational record was utilized to define the target distribution. Under the assumption of stationarity for the historical period, maximizing the sample size is crucial to ensure statistical robustness.

As a preliminary step to the derivation of the analytical curves, Figure 10 compares the Depth-Duration-Frequency (DDF) curves, analogous to IDF curves but expressing rainfall depth, derived from observed data against those obtained from the CPM historical simulation (shown here using L-Moments parameters as a representative example). This comparison visually underscores the critical necessity of applying bias correction. As evidenced by the plot, the raw climate model output significantly underestimates the precipitation extremes compared to the observations.

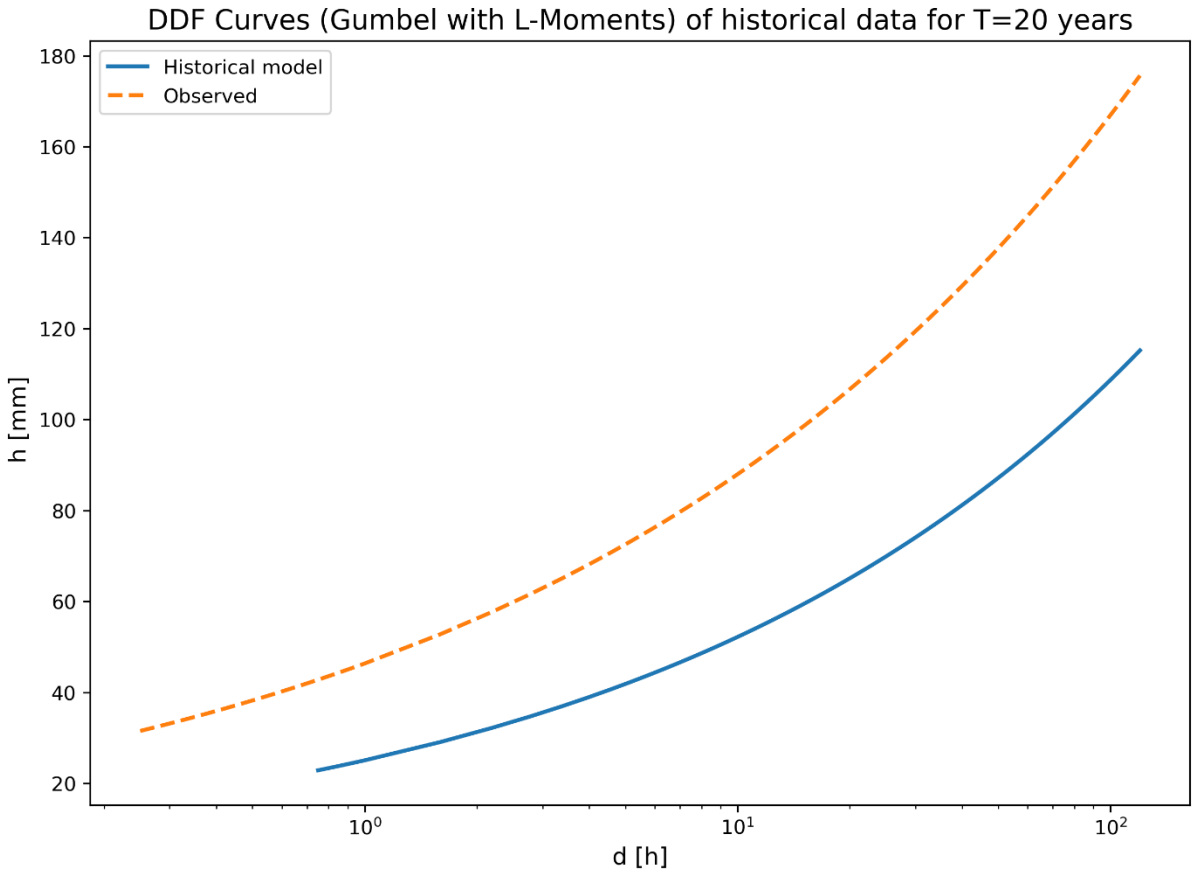

Figure 10: DDF Curves obtained from Gumbel L-Moments AMS of observed and historical model dataset.

Once the bias has been calibrated over a historical reference period ($Eq.(29)$), the quantile mapping relationship is applied to future model simulations by assuming that the statistical bias identified in the historical period remains stationary in time, as computed in $Eq.(30)$. This approach ensures that future precipitation projections are corrected using the same statistical relationship identified under present-day climate conditions, thus preserving the climate change signal simulated by the model while accounting for systematic biases.

$$P^*_{mod,hist} = F^{-1}_{obs}\left(F_{mod,hist}\left(P_{mod,hist}\right)\right) \qquad Eq.(29)$$

$$P^*_{mod,fut} = F^{-1}_{obs}\left(F_{mod,hist}\left(P_{mod,fut}\right)\right) \qquad Eq.(30)$$

To ensure methodological consistency, the quantile mapping procedure was performed separately for each parameter estimation method. The transfer functions were derived first using the CDFs fitted via L-Moments, and subsequently using those fitted via MLE. This generated two distinct corrected datasets, ensuring that the final IDF curves for each method were based on a coherent statistical correction process.

3.3.3. IDF curves fitting

Following the selection of the probability distribution, the next step involved determining the rainfall depths for the return period of interest. This study considered T = 2, 5, 10, 20, and 50 years. For each return period, the corresponding non-exceedance probability p was calculated through $Eq.(22)$. The specific rainfall depth associated with this probability was then extracted from the inverse of the CDF for each duration, providing a set of discrete points for the DDF curve.

To define the final design parameters (a and n) for the hydraulic simulations, an ensemble averaging approach was implemented prior to the regression analysis. The discrete rainfall depths were initially calculated using both MLE and L-Moments estimators. Subsequently, these values were averaged for each duration step to filter out method-specific biases. The power law relationship was then fitted directly to these ensemble-averaged discrete points, yielding a unique and robust analytical formulation for the IDF curves.

To derive a continuous curve, the power law relationship becomes linear in the bi-logarithmic plot, allowing the parameter a to be identified as the intercept (representing the rainfall depth for d=1 h), and n as the slope of the line, as defined in $Eq.(31)$.

$$ln(h) = ln(a) + n \cdot ln(d) \qquad Eq.(31)$$

Figure 11 illustrates the resulting continuous DDF curves overlaid on the discrete points. The goodness-of-fit is generally high, particularly for lower return periods, as evidenced by the r-squared value (R^2) in Table 3. However, a slight decrease in R^2 is observed as the return period increases. This phenomenon is attributable to the amplification of statistical uncertainties in the distribution tails [36].

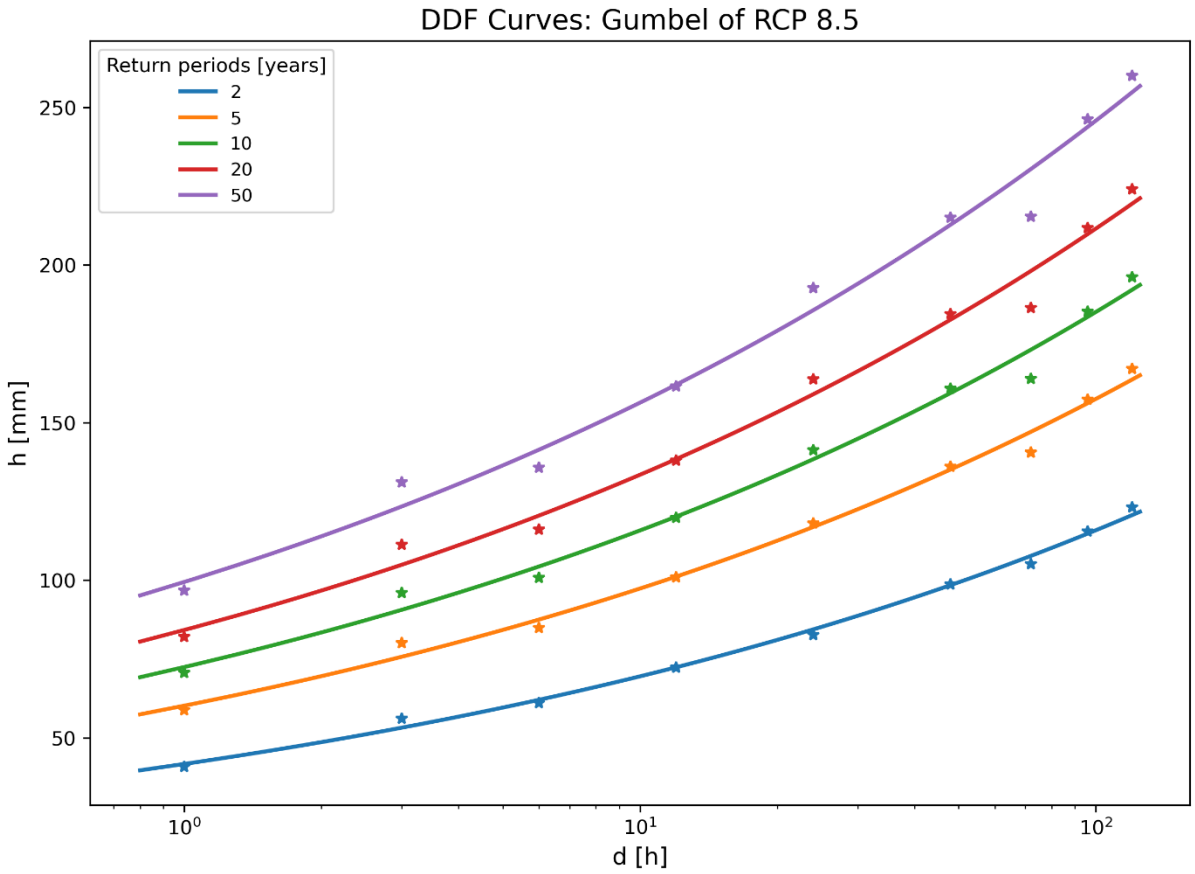

Figure 11: DDF Curves obtained from the averaged RCP 8.5 future corrected data points (MLE and L-Moments).

Table 3: Power law fitting parameters and fitting quality for different return periods. Values reported for the averaged DDF curves of RCP 8.5

T [years]	a [mm]	n [-]	R^2
2	41.70	0.222	0.996
5	60.19	0.209	0.993
10	72.45	0.204	0.990
20	84.21	0.200	0.988
50	99.44	0.197	0.986

3.3.4. Comparison of IDF Curves

The comparison between the historical rainfall data and the future climate projections reveals a significant intensification of extreme events. This trend is visually presented in Figure 12, which displays the final design IDF curves for both future scenarios (RCP 4.5 and RCP 8.5), derived by averaging the MLE and L-Moments projections, and the historical observed IDF curves with both fitting methods of the Gumbel distribution. Additionally, the historical IDF curve from the MISP project is included as the reference baseline used for the original drainage network sizing. To ensure

clarity, only the curves corresponding to a return period of T=10 years are plotted. It is important to note that the dashed sections of the lines represent the extrapolation range derived from the power law equation, which includes durations not involved in the parameters estimation.

Furthermore, as mentioned in Section 3.2.1, the observed dataset is characterized by a limited historical data record for short durations (approximately 10 years). Consequently, the statistical estimates for sub-hourly durations are characterized by a higher degree of uncertainty compared to hourly durations. However, since the definition of rainfall intensity at a sub-hourly scale is necessary for the hydraulic assessment, as later described, the curves in this range should be interpreted with caution regarding their statistical robustness.

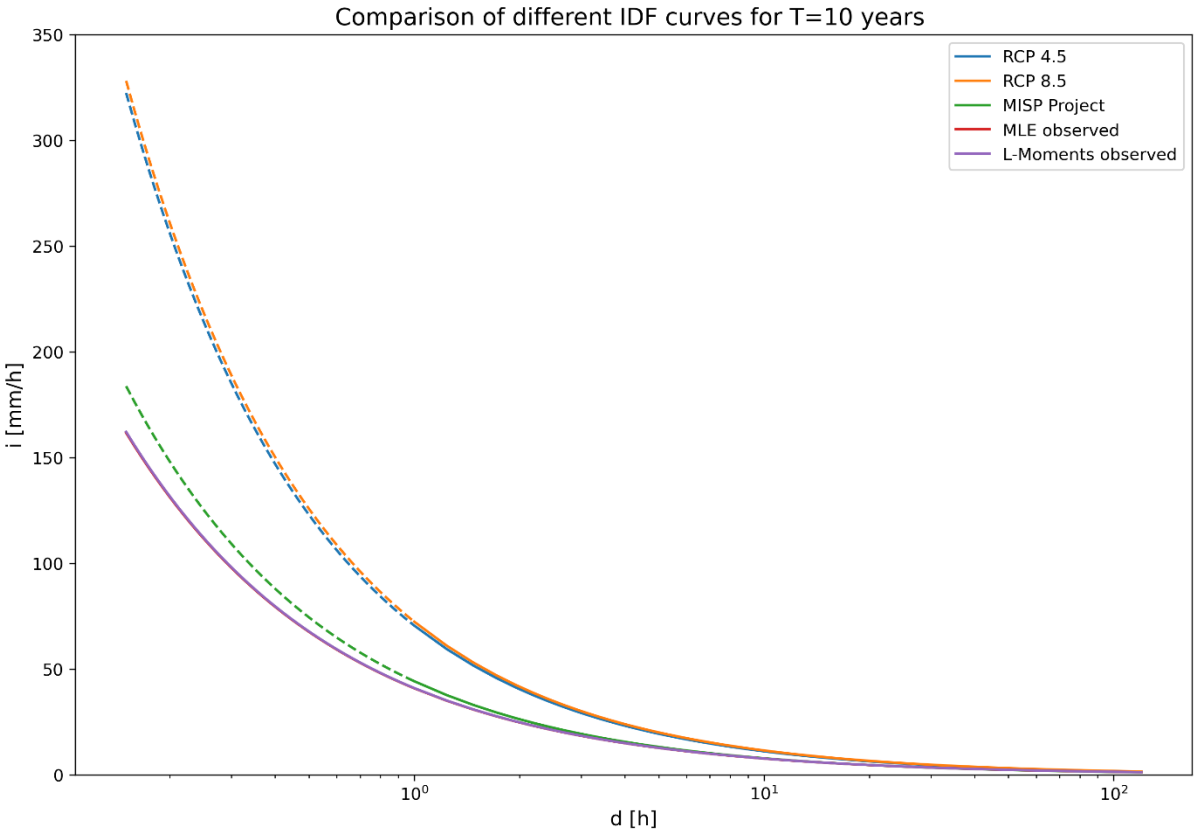

Figure 12: IDF Curves obtained from historical observed (MLE and L-Moments) and future scenarios with Gumbel distribution.

All future curves exhibit a generalized upward shift compared to the MISP project baseline. However, the magnitude of this shift is heavily dependent on the statistical approach. Interestingly, the projections for RCP 4.5 and RCP 8.5 appear remarkably similar in magnitude, suggesting that for the near-future horizon (or specifically for this local context), the signal of intensification is consistent regardless of the emission scenario.

To quantify this intensification, Figure 13 shows the percentage increase of future intensity relative to the historical baseline used in the design of the drainage network (MISP project). Firstly, it is

evident that the climate change signal is not constant across all time scales, with the relative increase being most pronounced for short durations.

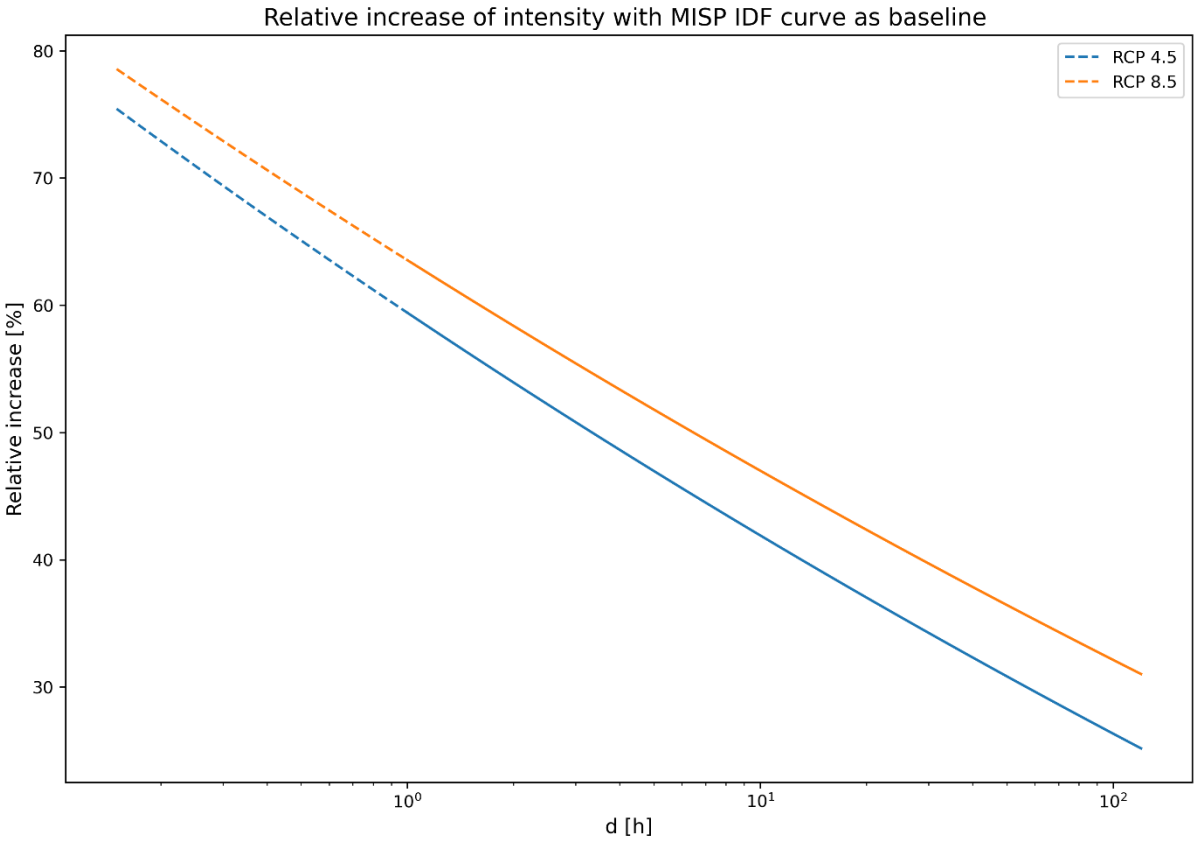

Figure 13: Percentage increase of the future intensity relative to the MISP project baseline.

Focusing on the hourly intensity (d = 1 h), the average projection estimates an increase of approximately +60% and +64% for future RCP 4.5 and RCP 8.5 scenarios, respectively.

3.3.5. Hydrological Analysis and Cost Evaluation

Now that IDF curves are available, it's possible to move on to the drainage system analysis of the MISP project. Figure 14 summarizes the steps involved in the design of the drainage network, which will be better described after.

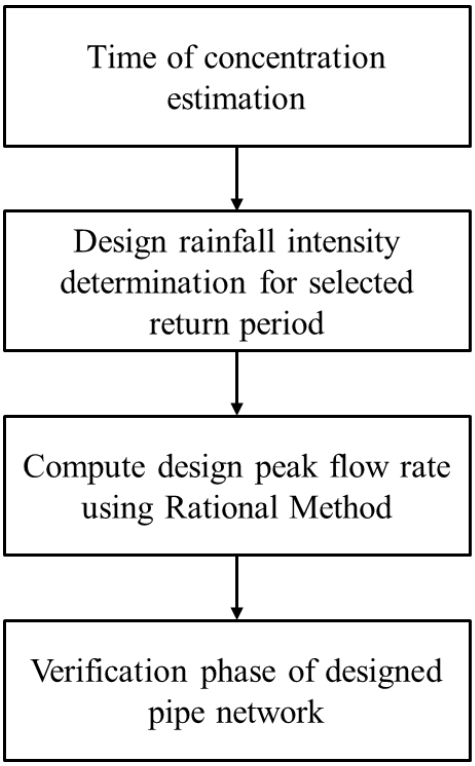

Figure 14: Steps in the hydraulic analysis of the drainage network.

The transformation of rainfall intensity into design discharge was performed using the Rational method as [37],

$$Q = \frac{\phi \cdot i_c \cdot S}{3600}\ , \qquad Eq.(32)$$

where:

- Q: maximum flow rate of runoff in l/s;
- i_c: design rainfall intensity in mm/h;
- S: area of the basin in m^2;
- ϕ: runoff coefficient. It expresses the permeability of the surface involved in the drainage system. In this study, since there's a concrete pavement, a runoff equal to 1 will be employed.

The design of the stormwater network was carried out considering a return period of T = 10 years, for which the corresponding power law parameters were obtained (see Table 4). This choice complies with the technical standards set by the "*Piano Regolatore del Porto di Trieste - Relazione Idraulica*" [38].

Table 4: Power law fitting parameters for averaged Gumbel distribution for T=10 years

	Historical	**Future RCP 4.5**	**Future RCP 8.5**
a	40.95	70.62	72.45
n	0.276	0.220	0.204

For each section of the network, the design rainfall intensity was determined considering a duration of the extreme event equal to the time of concentration, which is associated to the maximum flow rate [39]. As a definition, time of concentration is the time required from the runoff water to flow from the hydraulically most distant point in the watershed to the outlet. It is evaluated considering the entry time t_e, so the longest time required by the water to travel on the concrete pavement, and the travel time t_{net}, i.e. the longest time withing the pipe network, defined as the pipe section length L and the flow velocity V (see $Eq.(33)$)

$$t_c = t_e + t_{net} = t_e + \frac{L}{V} \qquad Eq.(33)$$

Values of t_e and V were assumed based on experience and literature, corresponding to 5 min and 1 m/s (flat areas) respectively [28].

In any case, a minimum duration of 10 minutes was considered for the intensity evaluation, otherwise shorter event durations would strongly overestimate real intensities, whose equation parameter were estimated based on longer durations [40]. Considering the above assumptions and the moderate length of the pipes, the time of concentration, and so duration, resulted almost always below 10 minutes. The previous analysis was applied to each basin and sub-basin contributing to each section of the drainage system. Since 229 pipe sections are present, only a short excerpt of the results is reported in Table 5, in this case with the evaluation of the design rainfall intensity with historical parameters in Table 4.

Table 5: Excerpt of results obtained by applying Rational Method to historical case

Network	S [m^2]	ϕ	L [m]	t_{net} [min]	t_c [min]	d [min]	i_c [mm/h]	Q [l/s]
B1/1-2,01->B1/1-1,03	681.8	1	9.3	0.16	5.16	10	150.36	28.48
B1/1-3,01->B1/1-1,04	749.9	1	9.3	0.16	5.16	10	150.36	31.32
B1/1-4,01->B1/1-1,05	804.2	1	9.3	0.16	5.16	10	150.36	33.59
B1/1-5,01->B1/1-1,06	858.3	1	9.3	0.16	5.16	10	150.36	35.85
B1/1-6,01->B1/1-1,07	865.5	1	9.3	0.16	5.16	10	150.36	36.15
B1/1-7,01->B1/1-1,08	870.4	1	10.2	0.17	5.17	10	150.36	36.35
B1/1-8,01->B1/1-8,02	657.5	1	26.6	0.44	5.44	10	150.36	27.46
B1/1-8,02->B1/1-8,03	1315	1	53.1	0.89	5.89	10	150.36	54.92
B1/1-8,03->B1/1-8,04	1972.5	1	79.7	1.33	6.33	10	150.36	82.39
B1/1-8,04->B1/1-8,05	2629.9	1	105	1.75	6.75	10	150.36	109.85
B1/1-8,05->B1/1-8,06	3287.4	1	128	2.13	7.13	10	150.36	137.31
B1/1-8,06->B1/1-1,08	3941.6	1	139.7	2.33	7.33	10	150.36	164.63

Given the peak flow rate, a diameter D for the pipe section is selected so that it can manage that flow rate.

Now it's necessary to hydraulically verify that the designed section can manage the peak flow rate. Considering uniform flow conditions, the Manning-Strickler equation, is used to estimate the design flow rate and is reported in $Eq.(34)$ [40].

$$Q_{design} = \frac{1}{n} \cdot A \cdot R^{\frac{2}{3}} \cdot s^{1/2} \ , \qquad Eq.(34)$$

where:

- k: Manning roughness coefficient.
- A: wet area of pipe section
- R: hydraulic radius, defined as the ratio between wet area and wetted perimeter WP (not including the free surface)
- s: slope of the pipe, fixed to 0.3% for all sections.

Considering that drainage network utilizes corrugated High-Density Polyethylene (HDPE) conduits with a smooth inner liner, a Manning's coefficient n=0.0125 was used, as performed in [28]. This design value lies between typical range 0.009-0.015 for smooth-lined polyethylene pipes [40].

Since the network operates under gravity flow conditions, the geometric characteristics of the wetted section vary as a function of the water level inside the pipe. A schematic representation is provided in Figure 15 to facilitate the understanding of the following geometric relationships [41].

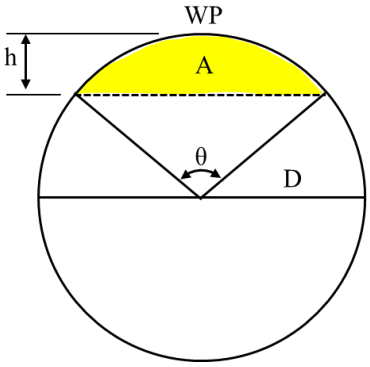

Figure 15: Geometry of a circular segment: relationship between radius, angle and height.

$$A = \frac{D^2}{8}(\theta - sin(\theta)) \quad , \qquad Eq.(35)$$

$$WP = \frac{D}{2}\theta \quad , \qquad Eq.(36)$$

$$R = \frac{A}{WP} = \frac{D}{4}\left(1 - \frac{sin(\theta)}{\theta}\right) \quad , \qquad Eq.(37)$$

$$f_r = \frac{h}{D} = \frac{1}{2}\left(1 - cos\left(\frac{\theta}{2}\right)\right) \qquad Eq.(38)$$

These equations were iteratively implemented by varying the angle θ until the calculated flow rate matched the peak flow rate generated by the rainfall event. If the resulting solution required θ>2π, it indicated that the pipe section was insufficient to convey the peak flow, necessitating the selection of a larger diameter.

Alternatively, the hydraulic verification could be performed by comparing the design peak flow rate Q_{peak} against the full-bore capacity Q_{full}, evaluated at θ=2π (pipe section completely full of water). Since previous equations were needed also to evaluate the filling ratio f_r, and Q_{full} doesn't represent the real maximum flow rate in a circular conduit, which is ≈7% higher and occurs at f_r≈94% due to reduction of wetted perimeter friction near the top of the pipe, it was decided to use angle θ as verification variable since it provides a more rigorous and complete methodology.

Table 6: Excerpt of verification results of historical case study

Network	D [mm]	n	A [mm^2]	R [mm]	Q [l/s]	θ [rad]	f_r [%]
B1/1-2,01->B1/1-1,03	300	0.00125	36	76	28.48	3.18	51%
B1/1-3,01->B1/1-1,04	300	0.00125	39	79	31.32	3.30	54%
B1/1-4,01->B1/1-1,05	300	0.00125	41	81	33.59	3.40	56%
B1/1-5,01->B1/1-1,06	300	0.00125	43	82	35.85	3.49	59%
B1/1-6,01->B1/1-1,07	300	0.00125	43	83	36.15	3.51	59%
B1/1-7,01->B1/1-1,08	300	0.00125	44	83	36.36	3.52	59%
B1/1-8,01->B1/1-8,02	300	0.00125	35	75	27.46	3.14	50%
B1/1-8,02->B1/1-8,03	400	0.00125	59	97	54.92	3.05	48%
B1/1-8,03->B1/1-8,04	400	0.00125	81	112	82.39	3.60	61%
B1/1-8,04->B1/1-8,05	500	0.00125	100	126	109.84	3.17	51%
B1/1-8,05->B1/1-8,06	500	0.00125	118	136	137.31	3.47	58%
B1/1-8,06->B1/1-1,08	600	0.00125	135	147	164.63	3.07	48%

In the historical analysis all pipe sections were satisfied, and no need of diameter correction was necessary. Results in Table 6 shows that pipe sections can easily manage the peak rainfall water flow due to low values of f_r. Considering the entire drainage network, the maximum filling ratio occurring is 70%.

Considering the pipe costs reported in Table 7, which were retrieved from the pipe supplier, it's possible to evaluate the cost of the entire drainage network.

Table 7: Pipe unit cost for each diameter used in the drainage network

D [mm]	Unit price [€/m]
250	19.94
300	24.94
400	42.24
500	61.74
600	96.73
700	117
800	157.64
900	185.72
1200	320.97

Established the hydraulic modelling framework and the geometric verification criteria, the study proceeds to assess the performance of the designed drainage network under projected climate conditions. While the physical characteristics of the network (pipe diameters, slopes, and layout)

remain fixed, the rainfall intensity is updated to reflect the climate change projections, whose parameters were reported in Table 4. Since drainage network remains fixed, also the time of concentration remains the same, so the duration of rainfall event (10 minutes minimum).

For each network section, the peak flow rate was recalculated using the Rational Method with the updated intensities. Subsequently, the hydraulic verification was repeated to evaluate the new filling ratios.

As expected, the verification phase allowed to identify many pipe sections with unrealistic values of θ, highlighted in red (θ>2π) in Table 8.

Table 8: Excerpt of results obtained to future scenarios with Gumbel distribution

		Future RCP 4.5			Future RCP 8.5		
Network	**D [mm]**	**i_c [mm/h]**	**Q [l/s]**	**θ [rad]**	**i_c [mm/h]**	**Q [l/s]**	**θ [rad]**
B1/1-2,01->B1/1-1,03	300	296.35	56.13	4.63	301.77	57.15	4.74
B1/1-3,01->B1/1-1,04	300	296.35	61.73	8.41	301.77	62.86	8.48
B1/1-4,01->B1/1-1,05	300	296.35	66.20	8.67	301.77	67.41	8.73
B1/1-5,01->B1/1-1,06	300	296.35	70.66	8.89	301.77	71.95	8.95
B1/1-6,01->B1/1-1,07	300	296.35	71.25	8.92	301.77	72.55	8.98
B1/1-7,01->B1/1-1,08	300	296.35	71.65	8.94	301.77	72.96	9.00
B1/1-8,01->B1/1-8,02	300	296.35	54.13	4.45	301.77	55.11	4.53
B1/1-8,02->B1/1-8,03	400	296.35	108.25	4.19	301.77	110.23	4.25
B1/1-8,03->B1/1-8,04	400	296.35	162.38	9.11	301.77	165.34	9.17
B1/1-8,04->B1/1-8,05	500	296.35	216.50	4.56	301.77	220.45	4.66
B1/1-8,05->B1/1-8,06	500	296.35	270.62	8.83	301.77	275.57	8.89
B1/1-8,06->B1/1-1,08	600	296.35	324.48	4.24	301.77	330.40	4.30

Figure 16 shows the fraction of network sections exhibiting hydraulic failure, meaning that the current hydraulic capacity is insufficient to cope with the projected climate change, indicating that a diameter upgrade is required.

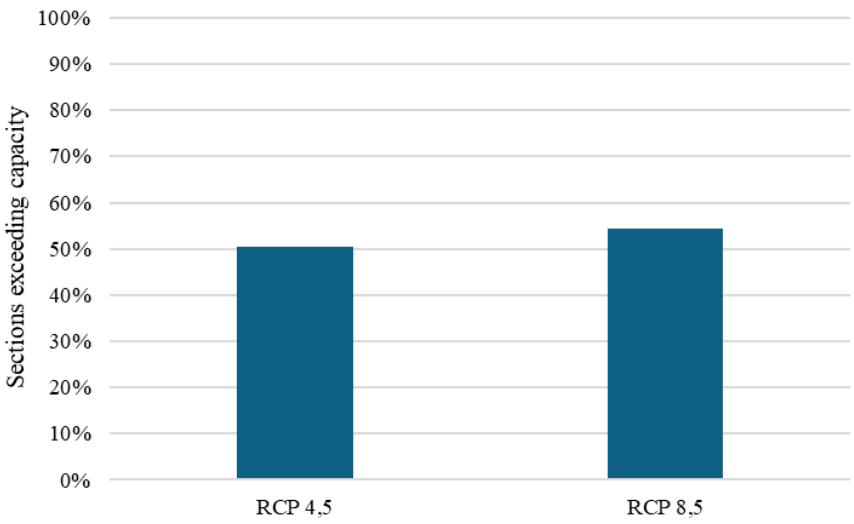

Figure 16: Number of drainage network sections requiring diameter upgrades (in %) due to hydraulic overload in future scenarios.

Given this, the nominal diameter exhibiting hydraulic failure was upgraded to the next commercially available size according to the manufacturer's catalogue (Table 7). Following the substitution, the hydraulic analysis was repeated to determine the new angle θ. If the upgraded section still failed, the procedure was repeated until a valid θ was achieved. In almost all the pipe sections the successive diameter of the catalogue was sufficient to satisfy the angle condition.

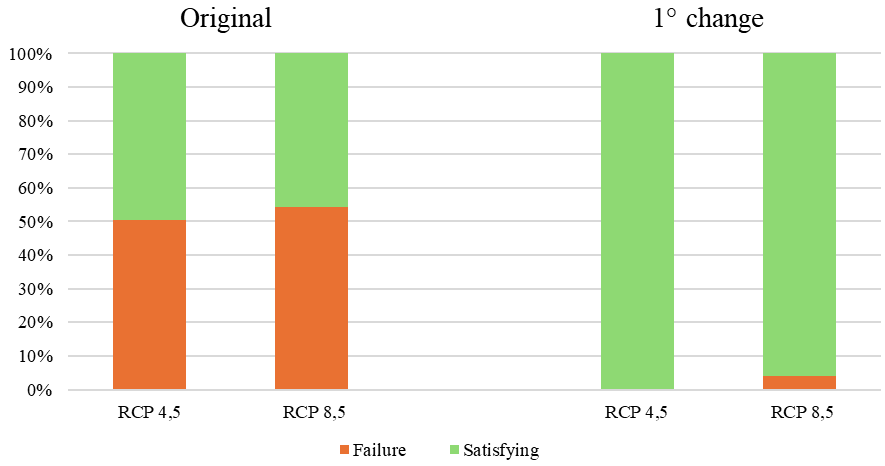

Figure 17: Summary of pipe sections modified and invariant for different future scenarios.

Figure 17 shows how much the failing network sections affect the entire system. On the left side, bars depict the initial status (consistent with Figure 16) distinguishing between the hydraulic compliant sections (invariant) and the critical ones (orange portion). The right bar displays the network status after applying a single-step diameter upgrade to the failing sections. The adaptation strategy was primarily calibrated to satisfy the requirements of the RCP 4.5 scenario, and subsequently tested under the more severe RCP 8.5 conditions.

The results demonstrate the effectiveness of the proposed adaptation strategy:

- RCP 4.5 Scenario: The upgrade of the 116 identified critical sections proves fully effectiveness. The critical status (orange bar) is completely eliminated in the post-intervention phase, indicating that a single-step diameter increase is sufficient to adapt the drainage system to the projected rainfall intensity.
- RCP 8.5 Scenario: Under this scenario, the network initially exhibited 125 failing sections (including the 116 identified in RCP 4.5 plus additional critical branches). Interestingly, applying the same structural upgrades designed for the RCP 4.5 scenario resulted in the resolution of 116 out of 125 cases. This indicates that, for the vast majority of the network, the hydraulic capacity gain provided by the standard commercial upsizing is sufficient to accommodate even the worst-case climate projections. However, a residual vulnerability persists in the remaining sections, where the increased rainfall intensity of RCP 8.5 requires a more substantial intervention compared to the RCP 4.5 design.

Cost of the drainage network was assessed based on unit costs reported in Table 7. The unit cost was applied to the entire length of pipe sections of that specific diameter, and then the overall cost was computed. Table 9 provides a quantitative breakdown of the network structure in terms of linear meters for each diameter D. The "Original" column reflects the current configuration of the drainage system, based on historical IDF curves. In contrast, the subsequent columns illustrate the extent of the structural upgrades, highlighting a clear shift towards larger diameters.

Table 9: Distribution of total pipe length by diameter, for original network and modified ones

	PIPE SECTIONS LENGTH [m]		
	Original	**Modified**	
D [mm]	Historical	RCP 4.5	RCP 8.5
250	372.4	48.1	48.1
300	727.6	780.7	780.7
400	1532.5	1377.0	1316.2
500	1248.6	1064.0	1124.7
600	536.8	871.0	847.1
700	516.9	385.3	409.1
800	493.3	413.1	374.7
900	0.0	488.9	527.4

Figure 18 translates the previous discussed table into economic terms, showing the total estimated cost for the network adaptation.

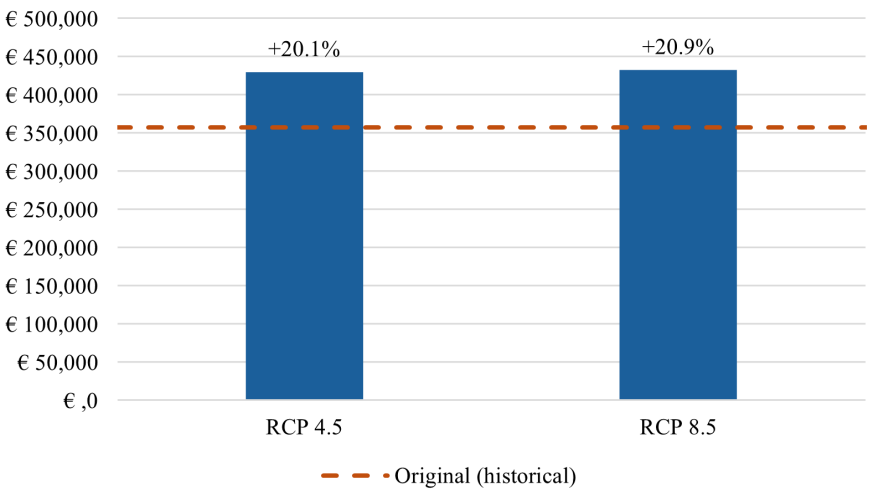

Figure 18: Estimated total drainage network costs under historical conditions (baseline) and future climate scenarios.

The graph compares the historical baseline cost of €357,550 against the projected costs for the two climate scenarios, calculated considering the average IDF curve for design rainfall intensity. To ensure the network complies with the intermediate climate projections, the estimated adaptation cost for the RCP 4.5 scenario rises to €429,500, representing an increase of +20.1% relative to the original infrastructure cost. This investment covers the upsizing of the 116 critical sections identified in the hydraulic analysis.

Under the worst-case emission scenario (RCP 8.5), the cost further increases to €432,300 (+20.9%). This additional financial burden reflects the need to address the residual vulnerabilities and the higher hydraulic stress imposed by the most severe rainfall projections.

Overall, the economic assessment confirms the significant financial scale of the challenge posed by non-stationary weather patterns. However, it is interesting to observe that the cost gap between the intermediate (RCP 4.5) and worst-case (RCP 8.5) scenarios is relatively contained. This finding aligns with the hydrological analysis presented in Section 3.3.4 which highlighted a consistent signal of intensification across both emission pathways.

From a planning perspective, this stability is a crucial result. Since the estimated investment is similar for both scenarios, the decision to upgrade the network becomes robust against future uncertainty.

4. Conclusions

This thesis addressed the critical challenge of designing and adapting urban drainage infrastructure to a non-stationary climate. By integrating high-resolution climate projections (VHR-PRO_IT) with advanced statistical modelling, the study quantified the impact of rainfall intensification on the drainage system of the MISP project in Trieste. The research moved from a theoretical assessment of climate data to a practical engineering application, providing a comprehensive workflow for resilient infrastructure design.

To derive robust design parameters, the study adopted a statistical averaging approach. The rainfall Intensity-Duration-Frequency (IDF) curves were generated by averaging the results estimated via Maximum Likelihood Estimation (MLE) and L-Moments. This methodological choice allowed to mitigate potential numerical instabilities associated with single estimators, providing a more stable basis for the hydraulic design compared to relying on a single fitting technique. The Gumbel distribution was selected as the reference model for the design process due to its superior performance in representing the examined datasets, as demonstrated by the Akaike Information Criterion (AIC) and Anderson-Darling (AD) tests against the GEV and Log-Normal distributions.

The analysis of future climate scenarios (RCP 4.5 and RCP 8.5) confirmed a significant intensification of extreme precipitation events compared to the historical baseline, which is particularly pronounced for short-duration events. Particularly, considering a design return period of 10 years, the design rainfall intensity is projected to increase by approximately +60% and +64% under the RCP 4.5 and RCP 8.5 scenario, respectively. Interestingly, for this specific climate model and location, the divergence between the two emission scenarios is limited, suggesting a strong and consistent signal of intensification that is largely independent of the specific emission trajectory in the near future.

The hydraulic simulations demonstrated that the existing drainage network, designed under the assumption of stationarity, is inadequate to cope with these projected extremes. Approximately 50% of the pipe sections exhibited hydraulic failure, with runoff flow rates exceeding the capacity of the pipe.

The proposed adaptation strategy, which involved upgrading the failing sections to the next commercially available diameter, proved highly effective.

Consequently, the upgrade implied a revision of the infrastructure costs. The estimated investment for adapting the network to the RCP 4.5 scenario corresponds to an increase of +20.1% compared to the original infrastructure, while the cost for the RCP 8.5 scenario is slightly higher (+20.9%).

While this study presents a flexible methodology that can be used for adaptation, it relies on a specific climate model (VHR-PRO_IT). This selection was driven by the current data availability, for which,

VHR-PRO_IT represents the only open-access Convection-Permitting Model (CPM) available with a 2.2 km resolution for the Italian territory. To further validate these findings and better quantify the epistemic uncertainty, future research should adopt a multi-model ensemble approach. As climate modelling evolves and more CPMs become available, using an ensemble of CPMs is recommended. This would generate a probabilistic range of design outcomes rather than deterministic values. Specifically, an ensemble approach would provide important information regarding the variability of the rainfall intensity estimates and, consequently, translate it into a corresponding range of adaptation costs. Ultimately, this would enable a more comprehensive assessment of climate risks and support robust financial planning for urban infrastructure.

REFERENCES

[1] Intergovernmental Panel on Climate Change (IPCC), "Water Cycle Changes," in *Climate Change 2021 – The Physical Science Basis*, Cambridge University Press, 2023, pp. 1055–1210. doi: 10.1017/9781009157896.010.

[2] K. E. Trenberth, A. Dai, R. M. Rasmussen, and D. B. Parsons, "The Changing Character of Precipitation," *Bull. Amer. Meteor. Soc.*, vol. 84, pp. 1205–1218, 2003, doi: 10.1175/BAMS-84-9-1205.

[3] J.-L. Martel, F. P. Brissette, P. Lucas-Picher, M. Troin, and R. Arsenault, "Climate Change and Rainfall Intensity–Duration–Frequency Curves: Overview of Science and Guidelines for Adaptation," *J. Hydrol. Eng.*, vol. 26, no. 10, Oct. 2021, doi: 10.1061/(asce)he.1943-5584.0002122.

[4] C. Wasko *et al.*, "A systematic review of climate change science relevant to Australian design flood estimation," Mar. 15, 2024, *Copernicus Publications*. doi: 10.5194/hess-28-1251-2024.

[5] P. C. D. Milly *et al.*, "Climate change: Stationarity is dead: Whither water management?," Feb. 01, 2008. doi: 10.1126/science.1151915.

[6] I. B. Gregersen, "Past, present and future variations of extreme rainfall in Denmark," Technical University of Denmark, DTU Environment, 2015.

[7] R. W. Katz, "Extreme value theory for precipitation: sensitivity analysis for climate change," *Adv. Water Resour.*, 1999, doi: 10.1016/S0309-1708(99)00017-2.

[8] M. Self, "Precipitation Analysis Using Extreme Value Theory," 2023. [Online]. Available: https://www.soa.org/49496b/globalassets/assets/files/resources/research-report/2023/2023-precipitation-extreme-value-theory.pdf

[9] N. Reid, "Statistical Sufficiency," in *International Encyclopedia of the Social & Behavioral Sciences*, N. J. Smelser and P. B. Baltes, Eds., Oxford: Pergamon, 2001, pp. 15044–15049. doi: https://doi.org/10.1016/B0-08-043076-7/00516-7.

[10] T. S. Gubareva, "Types of probability distributions in the evaluation of extreme floods," *Water Resources*, vol. 38, no. 7, pp. 962–971, Dec. 2011, doi: 10.1134/S0097807811070074.

[11] I. O. Palacios, "Introduction to statistical modeling of extreme values," Universidad Zaragoza, 2017. [Online]. Available: https://zaguan.unizar.es/record/64263/files/TAZ-TFG-2017-2126.pdf

[12] W. Huang, S. Xu, and S. Nnaji, "Evaluation of GEV model for frequency analysis of annual maximum water levels in the coast of United States," *Ocean Engineering*, vol. 35, no. 11–12, pp. 1132–1147, Aug. 2008, doi: 10.1016/j.oceaneng.2008.04.010.

[13] E. L. Crow and K. Shimizu, "Lognormal Distributions - Theory and Applications," 1988, [Online]. Available: https://www.researchgate.net/profile/Brian-Dennis-2/publication/313876706_Applications_in_Ecology/links/58ac8c3f92851c3cfda05623/Applications-in-Ecology.pdf

[14] P. Ailliot, C. Thompson, and P. Thomson, "Mixed methods for fitting the GEV distribution," *Water Resour. Res.*, vol. 47, no. 5, 2011, doi: 10.1029/2010WR009417.

[15] M. S. ul R. Khan *et al.*, "A comparative analysis of L-moments, maximum likelihood, and maximum product of spacing methods for the four-parameter kappa distribution in extreme value analysis," *Sci. Rep.*, vol. 15, no. 1, Dec. 2025, doi: 10.1038/s41598-024-84056-1.

[16] J. R. M. Hosking, J. R. Wallis, and E. F. Wood, "Estimation of the Generalized Extreme-Value Distribution by the Method of Probability-Weighted Moments," *Control TECHNOMETRICS*, vol. 27, no. 3, 1985, doi: 10.1080/00401706.1985.10488049.

[17] D. Bílková, "Lognormal distribution and using L-moment method for estimating its parameters," *International Journal of Mathematical Models and Methods in Applied Sciences*, vol. 6, no. 1, 2012, [Online]. Available: https://naun.org/main/NAUN/ijmmas/17-079.pdf

[18] F. Laio, G. Di Baldassarre, and A. Montanari, "Model selection techniques for the frequency analysis of hydrological extremes," *Water Resour. Res.*, vol. 45, no. 7, Jul. 2009, doi: 10.1029/2007WR006666.

[19] C.-Q. Li and W. Yang, "Time-dependent reliability methods," in *Time-Dependent Reliability Theory and Its Applications*, Elsevier, 2023, pp. 121–182. doi: 10.1016/b978-0-323-85882-3.00001-5.

[20] E. Gilleland and R. W. Katz, "ExtRemes 2.0: An extreme value analysis package in R," *J. Stat. Softw.*, vol. 72, Jan. 2016, doi: 10.18637/jss.v072.i08.

[21] A. Forestieri, E. Arnone, S. Blenkinsop, A. Candela, H. Fowler, and L. V. Noto, "The impact of climate change on extreme precipitation in Sicily, Italy," *Hydrol. Process.*, vol. 32, no. 3, pp. 332–348, Jan. 2018, doi: 10.1002/hyp.11421.

[22] R. Laprise, "Regional climate modelling," *J. Comput. Phys.*, vol. 227, no. 7, pp. 3641–3666, Mar. 2008, doi: 10.1016/j.jcp.2006.10.024.

[23] M. Raffa *et al.*, "Very High Resolution Projections over Italy under different CMIP5 IPCC scenarios," *Sci. Data*, vol. 10, no. 1, Dec. 2023, doi: 10.1038/s41597-023-02144-9.

[24] G. Lazoglou *et al.*, "Multivariate adjustment of drizzle bias using machine learning in European climate projections," *Geosci. Model Dev.*, vol. 17, no. 11, pp. 4689–4703, Jun. 2024, doi: 10.5194/gmd-17-4689-2024.

[25] Copernicus Climate Change Service, "What is bias correction?" [Online]. Available: https://climate.copernicus.eu/sites/default/files/2021-01/infosheet7.pdf

[26] T. Lafon, S. Dadson, G. Buys, and C. Prudhomme, "Bias correction of daily precipitation simulated by a regional climate model: A comparison of methods," *International Journal of Climatology*, vol. 33, no. 6, pp. 1367–1381, May 2013, doi: 10.1002/joc.3518.

[27] L. Gudmundsson, J. B. Bremnes, J. E. Haugen, and T. Engen Skaugen, "Technical Note: Downscaling RCM precipitation to the station scale using quantile mapping – a comparison of methods," May 15, 2012. doi: 10.5194/hessd-9-6185-2012.

[28] P. G. Fenaroli, "Progetto Di MISP Area Ex Ferriera Di Servola: Acque Meteoriche - Relazione Idraulica E Idrologica," 2024.

[29] OpenStreetMap, "uMap." Accessed: Feb. 14, 2026. [Online]. Available: https://umap.openstreetmap.fr/it/about/

[30] Arpa FVG, “Le Precipitazioni In Friuli Venezia Giulia - Schede Climatiche,” 2023. [Online]. Available: www.meteo.fvg.it

[31] Regione Autonoma Friuli Venezia Giulia, “Rete monitoraggio quantitativo acqua.” Accessed: Dec. 01, 2025. [Online]. Available: https://asr-str01.regione.fvg.it/PubblicazioneUOI/RicercaUOI.jsp

[32] Regione Autonoma Friuli Venezia Giulia, “Interpretazione dei dati idrologici e meteorologici del database territoriale.” [Online]. Available: https://www.regione.fvg.it/rafvg/export/sites/default/RAFVG/ambiente-territorio/tutela-ambiente-gestione-risorse-naturali/FOGLIA205/allegati/Interpretazione_dei_dati_idrologici_e_meteorologici.pdf

[33] S. M. Papalexiou, Y. G. Dialynas, and S. Grimaldi, “Hershfield factor revisited: Correcting annual maximum precipitation,” *J. Hydrol. (Amst).*, vol. 542, pp. 884–895, Nov. 2016, doi: 10.1016/j.jhydrol.2016.09.058.

[34] G. Ragulina and T. Reitan, “Generalized extreme value shape parameter and its nature for extreme precipitation using long time series and the Bayesian approach,” *Hydrological Sciences Journal*, vol. 62, no. 6, pp. 863–879, Apr. 2017, doi: 10.1080/02626667.2016.1260134.

[35] E. Ragno, A. AghaKouchak, C. A. Love, L. Cheng, F. Vahedifard, and C. H. R. Lima, “Quantifying Changes in Future Intensity-Duration-Frequency Curves Using Multimodel Ensemble Simulations,” *Water Resour. Res.*, vol. 54, no. 3, pp. 1751–1764, Mar. 2018, doi: 10.1002/2017WR021975.

[36] Y. Wang and E. McBean, “Uncertainty Characterization of Rainfall Inputs used in the Design of Storm Sewer Infrastructure,” *Journal of Water Management Modeling*, 2014, doi: 10.14796/JWMM.C367.

[37] DAKOTA GROUP, “Drainage Calculations and Flow Rates: How to Calculate Rainwater Flow Accurately.” Accessed: Feb. 04, 2026. [Online]. Available: https://academy.dakota.eu/en/drainage-flow-rate-calculation-why-it-matters

[38] F. Mattarolo, “PIANO REGOLATORE DEL PORTO DI TRIESTE - Studio Ambientale Integrato,” 2014. [Online]. Available: https://va.mite.gov.it/File/Documento/114173

[39] SUDAS, “SUDAS Design Manual - Chapter 2,” 2013. [Online]. Available: https://www.iowasudas.org/manuals/design-manual/

[40] C. Thomason, “Hydraulic Design Manual,” 2019. [Online]. Available: https://www.txdot.gov/manuals/des/hyd/index.html

[41] E. W. Weisstein, “Circular Segment”, Accessed: Feb. 07, 2026. [Online]. Available: https://mathworld.wolfram.com/CircularSegment.html